

# 3D Reconstruction of the Human Colon from Capsule Endoscope Video

Pål Anders Floor, Ivar Farup, Marius Pedersen.

**Abstract**—As the number of people affected by diseases in the gastrointestinal system is ever-increasing, a higher demand on preventive screening is inevitable. This will significantly increase the workload on gastroenterologists. To help reduce the workload, tools from computer vision may be helpful. In this paper, we investigate the possibility of constructing 3D models of whole sections of the human colon using image sequences from wireless capsule endoscope video, providing enhanced viewing for gastroenterologists. As capsule endoscope images contain distortion and artifacts non-ideal for many 3D reconstruction algorithms, the problem is challenging. However, recent developments of virtual graphics-based models of the human gastrointestinal system, where distortion and artifacts can be enabled or disabled, makes it possible to “dissect” the problem. The graphical model also provides a ground truth, enabling computation of geometric distortion introduced by the 3D reconstruction method. In this paper, most distortions and artifacts are left out to determine if it is feasible to reconstruct whole sections of the human gastrointestinal system by existing methods. We demonstrate that 3D reconstruction is possible using simultaneous localization and mapping. Further, to reconstruct the gastrointestinal wall surface from resulting point clouds, varying greatly in density, Poisson surface reconstruction is a good option. The results are promising, encouraging further research on this problem.

**Index Terms**—3D reconstruction, capsule endoscopy, structure from motion, SLAM.

## I. INTRODUCTION

**NOTE:** This is a preliminary version of this paper. The final complete paper is to be found in IEEE ACCESS, Volume 13, DOI: 10.1109/ACCESS.2025.3587596 [1].

Severe diseases in the gastrointestinal (GI) system like Crohn’s disease, inflammatory bowel disease, and cancer, are reducing peoples quality of life, some leading to premature death. One way to detect such diseases at an early stage, reducing the risk of severe complications, is to make screening of the GI system a common procedure beyond a certain age. However, fear of pain and difficulties caused by endoscopy is a major factor limiting the number of people screening themselves without clear symptoms [2].

This work was supported by the Research Council of Norway (RCN), under the project CAPSULE no.300031

All authors are with the Coloumlab, Department of Computer Science, Norwegian University of Science and Technology (NTNU), Gjøvik, Norway (e-mails: paal.anders.floor@ntnu.no, ivar.farup@ntnu.no, marius.pedersen@ntnu.no).

The wireless capsule endoscope (WCE) [3] is a pill-sized capsule that the patient swallows, and is a good alternative for preventive screening as it avoids the above-mentioned problem and is capable of reaching all parts of the GI system. The WCE carries at least one camera on board, recording video while traversing the GI system. However, current standard WCE’s have significantly lower resolution and frame rate than typical endoscopes, with images of low quality. The video is often over eight hours long, making it challenging for gastroenterologists to detect pathologies. With increasing demand on screening, tools that place less strain on the gastroenterologists and reduce time-use per patient are needed.

One method that may help gastroenterologists is a 3D model enhancing pathologies in the intestinal wall, making them easier to detect. A 3D model may also prove useful for planning of treatment. The inspiration for this approach comes from the positive feedback of using 3D reconstruction in gastrointestinal endoscopy [4] as well as in other medical applications [5]. Currently, 3D models are obtained through CT-scanning, which is expensive and may expose the patient to unnecessary radiation. Therefore, we will investigate the construction of 3D models based solely on WCE images. The approach in [6], making 3D models from single WCE images, got positive feedback from gastroenterologists, motivating further study of the problem.

There are at least two methods that may be applied in order to reconstruct the 3D structure of a scene based on WCE images: 1) *Direct methods*, like *shape from shading* (SfS), which recovers 3D structure based on geometric modelling of how light is reflected off relevant surfaces [7], here the GI wall. 2) *Feature-based methods* like *structure from motion* (SfM), which recovers 3D shapes from features captured in multiple views of the same scene [8]. SfS can reconstruct 3D shapes from only one image, while SfM needs at least two images.

With many images of the same rigid scene available, SfM can provide accurate 3D reconstruction. This is not necessarily easy to obtain from WCE images for the following reasons: i) Sometimes only one image is available due to rapid movement of the WCE, or debris in the intestine. ii) SfM assumes rigid motion, which is sometimes violated due to muscle contractions (*peristalsis*). iii) Sometimes the WCE position does not change enough from frame to frame to avoid degeneracies. In case i) direct methods, like SfS, have to be applied, as was done in [6]. In case ii) one can apply *non-rigid* SfM (NR-SfM) [9], [10] taking non-rigid scene movement into account. In case iii) a *simultaneous localization and mapping*

(SLAM) [11], [12] approach may be applied. SLAM utilizes the fact that camera position and 3D structure are obtained from SfM, and does SfM locally among *keyframes*, i.e., frames with significantly different poses. Therefore, SLAM can potentially detect and ignore frames leading to degeneracies.

A significant problem is that WCE images are of low quality. I.e., debris and bubbles in the intestinal fluids, specular reflections, motion blur, lens distortion, chromatic aberrations and compression artifacts are present in the images. This makes it very hard to design algorithms for accurate 3D reconstruction, as one cannot single out how each disturbance affect the reconstruction individually. However, with recent developments of virtual graphics-based models emulating the WCE traveling through the human GI system, one has the option to enable and disable most of the distortions and artifacts. It is then possible to “dissect” the problem and determine how each factor disturbs the reconstruction individually. One such model is VR-CAPS [13], which is a realistic looking artificial GI system built from CT scans of human intestines, where also the most typical corruptions in the WCE imaging process are modelled. Moreover, their GI-model can be exported and processed in 3D modelling tools, thereby providing a *ground truth* for evaluation of 3D reconstruction algorithms, something which is not possible for WCE.

In this paper, a feasibility study is conducted using an SfM-based SLAM approach for 3D reconstruction of whole sections of the human colon in an ideal situation where most of the distortions and artefacts are not present. To our knowledge, no other effort in the literature has dealt with this particular problem. The paper starts with our previous results from [14] computing point-clouds using typical WCE image resolution and frame-rate. These results show that 3D reconstruction using a feature-based approach is possible for the unusual and repetitive geometry of a typical colon. First SfM is investigated to gain basic knowledge, then this knowledge is applied to investigate a SLAM approach, named *ORB-SLAM* [12], which is a fast and accurate approach for monocular cameras. In extension of [14] the problem of surface reconstruction from the ORB-SLAM point clouds is addressed. This is not trivial as these point clouds have highly varying density, even lacking data in places. Therefore, triangulation methods, like Delaunay triangulation [15], leads to a ragged, non-continuous surface with *low-poly* effects in many places. However, decent results are obtained with *Poisson surface reconstruction* [16], which is a *multi-resolution* approach, providing detailed structure where the point cloud is dense, and a smoothed structure where the point cloud is sparse. Finally, the reconstructed model is aligned with ground truth to compute the geometric error between them. The impact of image resolution is also studied, having the current WCE standard at one extreme and the colonoscopy standard (the *gold standard*) at the other.

In Section II the problem formulation is given and the existing methods we apply for our experiments are described. Sections III and IV contain the novel results of this paper. In Section III experiment with SfM and ORB-SLAM is conducted to obtain 3D point clouds of human colon segments. In Section IV surface reconstruction and geometric error computations are considered. A summary and future research

ideas are given in Section V.

## II. PROBLEM FORMULATION AND METHODS

Direct methods usually rely on accurate radiometric information, whereas feature-based methods rely on *stable* image features. As a typical WCE has low-quality rendering, adapting its camera response over time [17], [18], accurate radiometric information is hard to obtain over image sequences. Therefore, a feature-based approach is considered here. The block diagram for the proposed method is given in Fig. 1. Each block

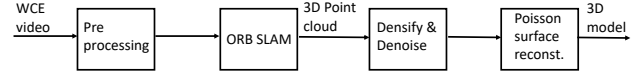


Fig. 1. Block diagram for computing 3D model of the GI system from WCE video.

will mainly consist of existing methods, which are described in the following subchapters and tailored to the problem at hand.

### A. VR-CAPS

VR-CAPS is a virtual environment for WCE [13] which is publicly available on github<sup>1</sup>. The environment is developed in *Unity*, a game development platform from *Unity Technologies*<sup>2</sup>. VR-CAPS emulates a range of organ types, capsule endoscopy designs, normal and abnormal tissue conditions as well as many other features detailed in [13]. The pixel resolution and frame rate can also be adjusted. Therefore, VR-CAPS enables testing of medical imaging algorithms both for current and future WCE designs.

The standard setup in VR-CAPS is a virtual colon model built from CT scans of a real human colon, covered with realistic looking textures. A section of this colon is depicted in Fig. 2(a) and an example image captured by the WCE inside this segment is depicted in Fig. 2(b). Many WCE models can

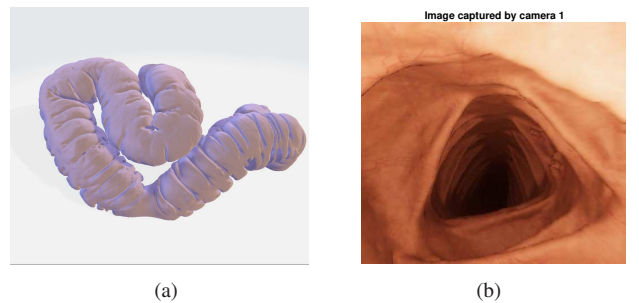


Fig. 2. (a) Section of colon from VR-CAPS applied for 3D reconstruction in this paper. (b) Example  $500 \times 500$  image taken by WCE inside the colon section in (a).

be simulated, but the default we use is a standard-sized pill with one camera and a spot-light with conical beam, emulating several LED’s surrounding the lens, a configuration often seen

<sup>1</sup><https://github.com/CapsuleEndoscopy/VirtualCapsuleEndoscopy> (Nov-21)

<sup>2</sup><https://unity.com/> (Nov-21)

in standard WCEs. We will use the standard setup for our experiments, but with varying pixel resolution, to evaluate its impact on the 3D reconstruction.

## B. Imaging Process

Generally, we assume that the image capturing process is some mapping between 3D projective space  $\mathbb{P}^3$  and 2D projective plane  $\mathbb{P}^2$ . Points in space,  $\mathbf{X}$ , are represented in *homogenous coordinates*  $\mathbf{X} = [X, Y, Z, W]^T$ , named *world coordinates*. Similarly, image points are represented as  $\mathbf{x} = [x, y, w]^T$ , named *image coordinates*. Here  $W, w \in \mathbb{R}^+$  are unspecified scaling factors [8, p. 7]. For 3D points in a *point cloud*  $\mathcal{X}$ , the  $i$ 'th point is denoted  $\mathbf{X}_i$ ,  $i = 1, \dots, N$ , and its image  $\mathbf{x}_i$ . The inhomogeneous coordinates,  $\tilde{\mathbf{X}}$  and  $\tilde{\mathbf{x}}$ , are related to the homogenous ones as [8, p. 65]

$$\tilde{\mathbf{X}} = [\tilde{X}, \tilde{Y}, \tilde{Z}] = \left[ \frac{X}{W}, \frac{Y}{W}, \frac{Z}{W} \right], \quad \tilde{\mathbf{x}} = [\tilde{x}, \tilde{y}] = \left[ \frac{x}{w}, \frac{y}{w} \right]. \quad (1)$$

With a *pinhole camera* the relation between a point  $\mathbf{X}_i$  and  $\mathbf{x}_i$  is a mapping  $P: \mathbb{P}^3 \rightarrow \mathbb{P}^2$ . For  $M$  views of a point,  $\mathbf{X}_i \in \mathcal{X}$ , the imaging process for the  $j$ 'th view is given by [8, p. 154]

$$\mathbf{x}_i^j = P^j \mathbf{X}_i, \quad j = 1, \dots, M, \quad i = 1, \dots, N, \quad (2)$$

where  $P^j$  is the  $3 \times 4$  *camera matrix* for the  $j$ 'th view given by [8, p. 156],

$$P^j = K[R^j | \mathbf{t}^j]. \quad (3)$$

$R^j$  is a  $3 \times 3$  rotation matrix and  $\mathbf{t}^j$ , a  $3 \times 1$  translation vector. In the WCE the same camera captures all views. Therefore, the *intrinsic matrix*,  $K$ , is the same for all views [8, p. 156]

$$K = \begin{bmatrix} fm_x & s & p_x m_x \\ 0 & fm_y & p_y m_y \\ 0 & 0 & 1 \end{bmatrix}, \quad (4)$$

where  $f$  is the *focal length*,  $p_x, p_y$  is the *principal point*,  $s$  is the *skew* and  $m_x, m_y$  is the number of pixels per unit distance in  $x$ - and  $y$  direction. The  $m_i$ -factors in  $K$  make Eq. (3) a transformation from world coordinates to *pixel coordinates*. For WCE's, usually  $s = 0$ . The other parameters can be found through a *calibration* procedure [8, p.226].

A simplifying assumption computationally is that the first view of any image sequence is taken by the camera when located at the world origin, i.e.,  $P^1 = K[I_{3 \times 3} | \mathbf{0}]$ , with  $I_{3 \times 3}$  the  $3 \times 3$  identity matrix. That is, camera coordinates of the first view are equivalent to world coordinates.

## C. Structure from Motion (SfM)

SfM recovers both 3D structure and individual camera poses. For two, three, or four views one can solve this using *tensors* namely *fundamental matrix* (FM), *trifocal tensor* and *quadrifocal tensor*, respectively [8]. These provide closed-form coordinate relations in terms of the camera matrices. For  $M > 4$  views one has to apply *bundle adjustment* (BA).

**1) Two views and the fundamental matrix:** Take Eq. (2) with  $M = 2$ . Then any two points  $\mathbf{x}_i^1, \mathbf{x}_i^2$ , being the images of  $\mathbf{X}_i$  in two views, are related by the *epipolar constraint* [8, p.245]

$$(\mathbf{x}_i^2)^T F \mathbf{x}_i^1 = 0, \quad \forall i, \quad (5)$$

with  $F$ , the FM, a  $3 \times 3$  rank 2 matrix given by  $F = [\mathbf{e}^2]_{\times} P^2 (P^1)^+$  [8, p.244]. Here  $\mathbf{e}^2$  is the *epipole*, the image of the camera center of view 1, and  $(P^1)^+$  is the Moore-Penrose pseudoinverse of  $P^1$ .  $A = [\mathbf{e}^2]_{\times}$  is a skew-symmetric matrix where  $a_{21} = e_3^2$ ,  $a_{31} = -e_2^2$ , and  $a_{32} = e_1^2$ .

$F$  can be estimated from common features in two images (like SIFT features). Features are generated in the two images and matches between them are searched. With  $n \geq 8$  such matches, the *normalized 8-point algorithm* can estimate  $F$  [8, p. 282]. With significant noise in the image, *outliers* can be problematic, and is usually dealt with by the RANSAC [19] algorithm. With  $F$  estimated, assuming that the camera center of the first view is at the world origin, the two camera matrices are given by  $P^1 = K[I | \mathbf{0}]$  and  $P^2 = [[\mathbf{e}^2]_{\times} F | \mathbf{e}^2]$  [8, p.256]. With  $P^1, P^2$  determined, one can estimate the related 3D point,  $\hat{\mathbf{X}}_i$ , for the correspondence  $\mathbf{x}_i^1 \leftrightarrow \mathbf{x}_i^2$ , satisfying the constraint (5), by a *triangulation method* [8, p. 311-313],  $\hat{\mathbf{X}}_i = \tau(\mathbf{x}_i^1, \mathbf{x}_i^2, P^1, P^2)$ .

With  $\hat{\mathbf{x}}_i^j$ , the projection of  $\hat{\mathbf{X}}_i$  in the  $j$ -th view, one minimizes the *reprojection error* [8, p. 314],  $C(\mathbf{x}_i^1, \mathbf{x}_i^2) = d(\mathbf{x}_i^1, \hat{\mathbf{x}}_i^1)^2 + d(\mathbf{x}_i^2, \hat{\mathbf{x}}_i^2)^2$ , subject to (5), with  $d(\cdot, \cdot)$  some distance measure.

With  $K$  known, one can estimate the *Essential Matrix* (EM)  $E = K^T F K$  [8, p. 257], instead of the FM, which is simpler to compute. With  $K$  and  $F$  (or  $E$ ) known, the 3D scene can be reconstructed up to a *similarity transform* [8, p. 272-273], i.e., a Euclidean reconstruction up to an unknown scaling factor. The exception is the *degenerate case*, which can occur when the camera centers and  $\mathbf{X}_i$  are co-linear (practically close to co-linear). Under pure rotation about the camera center, the degenerate case  $F = 0$  occurs. For WCE, degeneracies may occur due to both of these cases. To obtain a metric reconstruction, information about the size of some object in the scene is needed. An effort dealing with this for WCE application is [20].

**2) Multiple Views and Bundle Adjustment (BA):** For  $M > 4$  views, the problem has to be dealt with numerically through *bundle adjustment* (BA), which is a minimization problem on the form [8, p. 434],

$$\min_{\hat{P}^j, \hat{\mathbf{X}}_i} \sum_{i,j} d(\hat{P}^j \hat{\mathbf{X}}_i, \mathbf{x}_i^j), \quad j = 1, \dots, M \quad i = 1, \dots, N, \quad (6)$$

with  $d(\cdot, \cdot)$ , some distance measure, typically Euclidean norm. That is, BA is the reprojection error over all views and 3D points. BA requires a good initial estimate,  $\hat{P}^j, \hat{\mathbf{X}}_i$ , of camera poses and 3D points, typically obtained by computing the FM sequentially over pairs of neighboring images for all views in the sequence [8, p.453]. BA is costly to compute for large  $M$  [8, p. 435], a problem solved by ORB-SLAM.

## D. ORB-SLAM

3D reconstruction from WCE video streams may require hundreds of images. Then, SfM alone is inconvenient due to



computational complexity and the difficulty of keeping track of which features are visible in a given view. For this task, a SLAM approach is needed. As WCE video is a sequence of monocular images, an approach known to perform well for that case, namely *ORB-SLAM* [12], is considered.

ORB-SLAM performs SfM locally among keyframes, which are arranged as in a *co-visibility graph*, a weighted graph where each node is a key frame with all relevant information included (number of features, their *score*, adjacency information etc.). There are edges among keyframes with common features, with weights corresponding to the number of features they share. The local computation of camera poses and 3D geometry greatly reduces computational cost. A global optimization is also performed to fine-tune the position of camera poses. ORB-features are used throughout as they are significantly faster to compute than SIFT or SURF features. ORB-SLAM is done in three steps in addition to an initialization procedure. See [12] for details.

0) *Initialization*: One out of two methods are chosen based on the scene: i) A homography if the scene is plane, or low parallax. ii) A FM if the scene is not plane. With  $K$  known, the EM,  $E = K^T F K$ , is estimated. The choice between the two cases is done automatically.

1) *Tracking*: Localizes the pose of each frame w.r.t. the first view, which is at the world origin ( $P^1 = K[I|0]$ ), by matching ORB-features. It also decides if a given frame should be inserted as a key frame in the co-visibility graph. The poses are then optimized using BA in (6) over the  $P^i$ 's only. If tracking is lost, a *global re-localization* procedure is initiated.

2) *Local Mapping*: Processes new keyframes and performs local BA to obtain a sparse 3D reconstruction in the surroundings of the relevant pose. New correspondences for unmatched ORB-features are searched in keyframes directly connected in the co-visibility graph to triangulate new 3D points. If a key frame does not change significantly compared to other keyframes, or if it lacks good point matches, it is discarded.

3) *Loop Closure*: With every new key frame the algorithm searches for *loops*, i.e., if the camera re-visits previous parts of the scene. When a loop is detected, it can estimate *drifts* in scale and position, which is the essential step to minimize geometric errors.

### E. Poisson Surface Reconstruction

As will be seen in Section III, the point clouds resulting from WCE video are noisy and vary greatly throughout space. Then typical surface reconstruction methods like *Delaunay triangulation* [15] and  $\alpha$ -*shapes* [21] are non-ideal, creating low-poly effects and gaps in the reconstructed model.

*Poisson surface reconstruction* proposed by Kazhdan et al. [16] is a *multiresolution* method that is convenient for this problem. The objective is to find an *indicator function*,  $\chi$ , separating the inside and outside a 3D object  $M$ , given a set of points,  $\tilde{\mathbf{X}}_i$  in a point cloud  $\tilde{\mathcal{X}}$ ,

$$\chi_M(\tilde{\mathbf{X}}_i) = \begin{cases} 1, & \tilde{\mathbf{X}}_i \in M \\ 0, & \tilde{\mathbf{X}}_i \notin M. \end{cases} \quad (7)$$

The *isosurface* (level surface),  $\partial M$ , of  $\chi_M$  for some constant value, defines the boundary of the relevant 3D object and thereby its surface. With  $\mathbf{v} \approx \nabla \chi_M$ , the unit normals to  $\partial M$  for all  $\tilde{\mathbf{X}}_i \in \tilde{\mathcal{X}}$ , the following minimization problem determines the optimal  $\chi_M$

$$\min_{\chi_M} \|\nabla \chi_M - \mathbf{v}\|, \quad (8)$$

which is equivalent to the *Poisson equation*,  $\nabla^2 \chi_M = \nabla \cdot \mathbf{v}$ . The derivative of  $\chi_M$  is not defined. Therefore, it has to be convolved with some *smoothing function*,  $\tilde{F}(\tilde{\mathbf{Y}})$ . It is shown in [16] that

$$\nabla^2 \tilde{\chi}_M = \nabla(\chi_M * \tilde{F})(\tilde{\mathbf{Y}}) = \int_{\partial M} \tilde{F}(\tilde{\mathbf{Y}} - \tilde{\mathbf{X}}) \mathbf{n}_{\partial M}(\tilde{\mathbf{X}}) d\tilde{\mathbf{X}}, \quad (9)$$

where  $\mathbf{n}_{\partial M}(\tilde{\mathbf{X}})$  is the inward facing normal to  $\partial M$  at  $\tilde{\mathbf{X}}$ .

Given a set of oriented points (the normals can be found by the procedure in [22]),  $\tilde{\mathcal{X}}$ , one can partition  $\partial M$  into disjoint surface regions  $\mathcal{P}_{\mathbf{X}} \subset \partial M$ . Given a point  $\tilde{\mathbf{X}}_i \in \tilde{\mathcal{X}}$ , with  $\mathbf{n}_i$  the corresponding unit normal, (9) can be approximated as [16]

$$\nabla^2 \tilde{\chi}_M \approx \sum_{\tilde{\mathbf{X}}_i \in \tilde{\mathcal{X}}} |\mathcal{P}_{\mathbf{X}}| \tilde{F}(\tilde{\mathbf{Y}} - \tilde{\mathbf{X}}_i) \mathbf{n}_i(\tilde{\mathbf{X}}_i) = \mathbf{v}. \quad (10)$$

$\tilde{F}$  is typically a *Gaussian Filter*. Solving  $\nabla^2 \tilde{\chi}_M = \mathbf{v}$  directly is not possible as  $\mathbf{v}$  is non-conservative. A least squares solution must be found, i.e., by solving [16]  $\nabla^2 \tilde{\chi}_M = \nabla \cdot \mathbf{v}$ .

The implementation is built around an *octree*, a tree where each node, except leaf nodes, has 8 children, and all samples,  $\tilde{\mathbf{X}}_i \in \tilde{\mathcal{X}}$ , are located in leaf nodes. The space containing the object  $M$  is subdivided into 8 cubes at each level of the tree so that finer resolution is obtained at deeper levels. To each leaf node,  $o$ , there is an associated function  $F_o$ , typically approximating a Gaussian filter, whose width is adapted to the local sample resolution [16]. With  $D_t$ , the depth of the octree, the relevant space will be divided into  $8^{D_t}$  cubes. This leads to a multiresolution structure where points in sparse neighborhoods are located in leaf nodes high up in the tree, whereas points in dense neighborhoods are located further down. Details on the implementation can be found in [16, Sections 4.3-4.5].

### F. Point Cloud Alignment and Error Computation

To compute the reconstruction error, Horn's *absolute orientation* approach [23] is applied to align the the 3D reconstructed model with the ground truth colon from VR-CAPS.

Assume two coordinate systems, "left",  $\mathbf{r}_l$ , and "right",  $\mathbf{r}_r$ , which could be two coordinate representations of the same point cloud  $\tilde{\mathcal{X}}$ . With noise present, there will be errors when one representation is transformed to the other. Given the coordinates of  $n$  measured points in  $\tilde{\mathcal{X}}$ , the relationship between the two coordinate representations is  $\mathbf{r}_r = s \cdot R(\mathbf{r}_l) + \mathbf{r}_0$ , where  $\mathbf{r}_0$  is the translation,  $s$  the scaling, and  $R(\cdot)$  the rotation. With  $\mathbf{e}_i = \mathbf{r}_{r_i} - s \cdot R(\mathbf{r}_{l_i}) - \mathbf{r}_0$ , the error per point, the problem is to minimize

$$\bar{\mathbf{e}}_t = \sum_{i=1}^n \|\mathbf{e}_i\|^2, \quad (11)$$

It's convenient to refer measurements to the *centroids*,  $\mathbf{C}_l = \frac{1}{n} \sum_{i=1}^n \mathbf{r}_{l_i}$  and  $\mathbf{C}_r = \frac{1}{n} \sum_{i=1}^n \mathbf{r}_{r_i}$ , so that  $\mathbf{r}'_{l_i} = \mathbf{r}_{l_i} - \mathbf{C}_l$ , and  $\mathbf{r}'_{r_i} = \mathbf{r}_{r_i} - \mathbf{C}_r$ . The minimum of (11) with  $\mathbf{e}_i = \mathbf{r}'_{r_i} - s \cdot R(\mathbf{r}'_{l_i}) - \mathbf{r}'_0$ , and where  $\mathbf{r}'_0 = \mathbf{r}_0 - \mathbf{C}_r + s \cdot R(\mathbf{C}_l)$ , is obtained with  $\mathbf{r}_0 = \mathbf{C}_r - s \cdot R(\mathbf{C}_l)$ , and [23]

$$s = \frac{\sum_{i=1}^n \mathbf{r}'_{r_i} \cdot R(\mathbf{r}'_{l_i})}{\sum_{i=1}^n \|\mathbf{r}'_{l_i}\|^2}. \quad (12)$$

The problem is then to find the  $R(\cdot)$  minimizing  $\sum_{i=1}^n \|\mathbf{r}'_{r_i} - s \cdot R(\mathbf{r}'_{l_i})\|^2$ , which is equivalent to maximizing  $D = \sum_{i=1}^n \|\mathbf{r}'_{r_i} \cdot R(\mathbf{r}'_{l_i})\|^2$  over  $R$ . The problem is formulated using *quaternions*, as a closed form solution can be found [23]. With  $\hat{q} = q_0 + \mathbf{i}q_x + \mathbf{j}q_y + \mathbf{k}q_z$ , a *unit quaternion* ( $\hat{q} \cdot \hat{q} = 1$ ), with  $\mathbf{i}, \mathbf{j}, \mathbf{k}$  an orthonormal basis for the relevant 3D space, it is shown in [23] that the objective function  $D$  above, can be written

$$D = \sum_{i=1}^n (\hat{q} \hat{r}'_{l_i} \hat{q}^*) \cdot \hat{r}'_{r_i} = \sum_{i=1}^n (\hat{q} \hat{r}'_{l_i}) \cdot (\hat{r}'_{r_i} \hat{q}), \quad (13)$$

where  $\hat{q}^*$  is the *conjugate* of  $\hat{q}$  and  $\hat{r} = \mathbf{i}r_x + \mathbf{j}r_y + \mathbf{k}r_z$  is the *imaginary quaternion*. How to determine the max of (13) and the corresponding algorithm is given in [23, pp. 635-636].

### III. POINT CLOUD COMPUTATION, SIMULATION SETUP AND EXPERIMENTS

To determine how well one may reconstruct sections of a typical colon, we apply the VR-CAPS simulator in Section II-A, then try to reconstruct the model colon using the methods described in Section II as in the block diagram in Fig. 1 for different image resolutions.

The VR-CAPS simulator is applied through several subsets of the colon segment, shown in Fig. 2(a). These are depicted in Figs. 5(a), 6(a) and 7(a), and serve as ground truth for the example 3D reconstructions. The image size is varied in three steps to evaluate the impact of image resolution: i)  $500 \times 500$ , corresponding to many current pillcams (like PillCam COLON2) ii)  $800 \times 800$  iii)  $1500 \times 1500$ , which is close to colonoscopy standard. The corresponding focal lengths in pixel units,  $f_{m_i}$ , are 250, 400 and 750 respectively. The principal point is at the image center for all cases, i.e.,  $p_x m_x = p_y m_y = \text{resolution}/2$  (quadratic images). The frame rate is set to 20 fps for all cases. All distortion effects are disabled as default. However, some distortions are enabled in turn to evaluate the impact on the 3D reconstruction in Section III-A.

The WCE is controlled in VR-CAPS by key buttons and a mouse. A steady movement is difficult to obtain, therefore the resulting WCE trajectory becomes irregular and ragged, especially through sharp bends. However, this movement appears quite similar to that of a real WCE, and will therefore test ORB-SLAM's ability to cope with realistic movement.

#### A. Structure from motion

We begin with SfM on a short colon segment to gain knowledge into the workings of the algorithm, how to correctly tune and initialize, as well as determine distortions the algorithm is

sensitive to. This knowledge will be useful when considering ORB-SLAM, indicating what pre-processing steps are needed.

2-view and 6-view SfM are considered for  $500 \times 500$  resolution. Since  $K$  is known, the EM,  $E = K^T F K$ , is estimated. SURF features are used to estimate  $E$  (and thereby

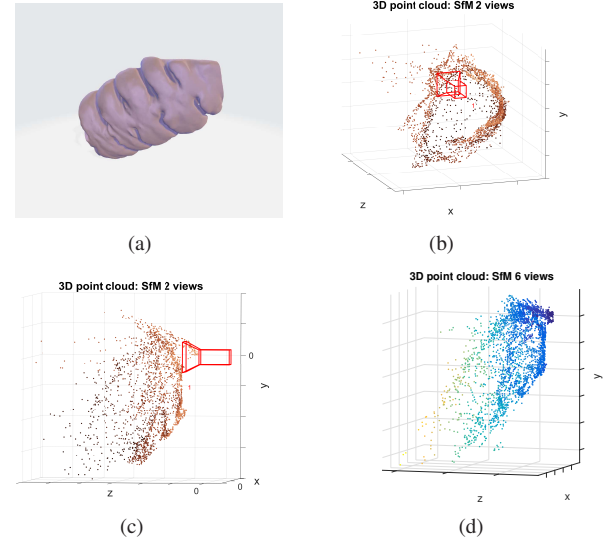


Fig. 3. Structure from Motion (SfM) 3D reconstruction (a) Ground truth colon segment (b) 2-view reconstruction seen from the front. (c) 2-view reconstruction seen from the side. (d) 6-views reconstruction seen from the side.

$P^i$ ) and the 3D points, whereas eigenfeatures are used to compute dense point clouds once  $E$  is known. For  $M = 6$  views, an initial reconstruction is made by sequentially computing  $E$  for pairs of consecutive frames (as in Algorithm 18.3 in [8, p. 453]) followed by BA. All relevant computation and estimation methods for our purposes are found in Matlab's *computer vision toolbox*<sup>3</sup>.

Based on experimentation on images from VR-CAPS, the following observations were made: i) Motion blur resulting from rapid rotations and panning of the WCE from image to image makes it hard to detect features. ii) Lens distortion makes the assumption of pinhole camera fail, and therefore leads to very sparse and inaccurate 3D point clouds. iii) Removal/inpainting of specs on lens and specular reflections is advantageous as they tend to confuse the feature detection algorithm. iv) As the WCE has a spotlight source, lighting will vary hugely across the image. Due to dim lighting, particularly in fields imaging deeper parts, contrast enhancement is essential to detect stable features. Due to the variation in brightness, we applied *adaptive histogram equalization*. Based on these findings, we suggest using the scheme shown in Fig. 4 for pre-processing in Fig. 1. The first block removes highly corrupted, blurry or content-less frames. The second block denoises and removes other disturbing artifact like specular reflections. The third block removes lens distortion, and the fourth enhances contrast to improve feature detection.

The colon segment we aim to reconstruct is shown in Fig. 3(a). The image seen in the first camera pose is depicted

<sup>3</sup><https://se.mathworks.com/products/computer-vision.html> (10/11-21)

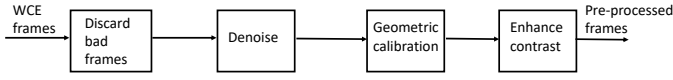


Fig. 4. Block diagram showing preprocessing for ORB-SLAM.

in Fig. 2(b), which is the reference for the 3D computation. The 2-view reconstruction is depicted in real color from the front and side in Figs. 3(b) and 3(c) respectively, with the first camera pose included. The 6-view reconstruction is shown in Fig. 3(d) from the side. The reconstruction is quite convincing, even with two images. The 6-view case is more accurate, as it rules out some outliers. Note in particular that the overall cylindrical shape of the colon in Fig. 3(a) is reconstructed quite well, indicating that perspective distortion is eliminated.

## B. ORB-SLAM

For long colon segments, a large number of views must be processed. ORB-SLAM is used for this purpose. All frames with significant motion blur are removed, as they make ORB-SLAM fail due to lack of feature matches. Further, it is assumed that lens distortion and other non-linearities have been compensated for so that a *pinhole model* can be assumed. It is also assumed that typical distortions seen in pillcam images, like debris on the lens, specular reflections etc. are taken care of through the pre-processing in Fig. 4.

1) *Algorithm for Densification*: As ORB-SLAM is optimized for fast computation and accurate localization, it produces a sparse point cloud containing 3D points of high accuracy needed to optimize camera localization. To make a denser point cloud for the purpose of surface reconstruction, the camera poses,  $P^i$ , and co-visibility graph,  $\mathcal{G}$ , obtained by ORB-SLAM are applied. The graph is traversed while computing dense SfM over sub-sets of keyframes as detailed in Algorithm III-B.1.

2) *Simulation Setup*: In initialization step 0) of ORB-SLAM (see section II-D) the algorithm is forced to choose an FM model as plane scenes never occur in the GI-system. Due to the WCE movement, initialization may then fail due to low parallax. If the initialization is rejected, then skip to the next frame and re-start the algorithm until the initialization succeeds. Loop closure (Step 3) should be disabled, as loops very seldom occur when the WCE travels through the GI system. The repetitive geometrical structure of the colon tends to confuse the ORB-SLAM algorithm, miss-interpreting these for being potential loop closure candidates. Without loop closure, one has to expect inaccuracies as scale and position will drift, particularly over longer segments. In sharp bends of the colon, drifts will be most noticeable due to large rotations of the camera. One can avoid scaling errors by running ORB-SLAM several times over different colon segments. In a real scenario, one would likely make 3D models only in segments of the colon surrounding pathologies. However, as the experiments below shows, increased image resolution enables longer segments to be reconstructed, indicating that future WCE's with higher image resolution should enable more accurate 3D reconstruction of longer colon segments.

---

### Algorithm 1 Densify ORB-SLAM point cloud

---

**Input:** Co-visibility graph  $\mathcal{G}$ , poses  $P^i = K[R_i|t_i]$ ,  $i = 1, \dots, N_{KF}$ , with  $N_{KF}$  number of nodes in  $\mathcal{G}$ .

**Output:**  $\mathcal{P}$  containing dense point cloud

**Initialize:** Point cloud object array  $\mathcal{A}$ , max number of views for dense reconstruction,  $M_V > 2$

```

for  $i = 1$  to  $N_{KF}$  do                                ▷ Loop through all keyframes
    Determine number of frames,  $N_{CV}$ , in  $\mathcal{G}$  sharing co-visibility features with keyframe no.  $i$  for  $j > i$ 
    if  $N_{CV} < M_V$  then
         $M_V \leftarrow N_{CV}$ 
        if  $M_V < 2$  then
             $\mathcal{A}(i) \leftarrow 0$ 
            Continue                                ▷ Jump to next iteration of loop
        end if
        Compute dense cloud,  $D$ , through  $M_V$ -view SfM, as in Section II-C, with dense features given  $P^j$ ,  $j = i, \dots, i + M_V - 1$ , with frame  $i$  as reference view
        if  $D$  has many outliers then                    ▷ Degeneracies
             $\mathcal{A}(i) \leftarrow 0$ 
            Continue                                ▷ Jump to next iteration of loop
        end if
         $\mathcal{A}(i) \leftarrow \text{denoise}^4 D$ 
    end if
end for
 $\mathcal{P} \leftarrow \text{concatenate clouds in } \mathcal{A} \text{ using } P^i, i = 1, \dots, N_{KF}$ 
  
```

---

ORB-features are detected under SLAM for computational efficiency. However, SURF and eigenfeatures are applied to compute the dense reconstruction in Algorithm III-B.1 as they seem to produce several more reliable features for colon geometry and texture. The same pre-processing as for SfM in Section III-A is assumed. The textures of the colon walls as well as its geometry are both crucial to obtain enough features to enable an adequate reconstruction. This leads to feature detection over a range of scales. To cover all relevant scales, at least 8 pyramid levels in the feature detection is needed.

3) *Experiments*: Three colon segment scenarios are considered: 1. Segments bending slowly. 2. Segments with sharp bends. 3. Long segments, covering about 30% of the colon. A 3D reconstruction approach of choice should at least be able to cope with the first two scenarios. A version of ORB-SLAM has been implemented by the MatLab community<sup>5</sup>, which we tailor to our purposes here.

**Scenario 1:** The colon segment under consideration is depicted in Fig. 5(a). For  $500 \times 500$  resolution, 996 images were generated of this segment in VR-CAPS, and 445 keyframes were chosen by the ORB-SLAM algorithm for reconstruction. For  $800 \times 800$  resolution, 863 images were generated, and 166 keyframes were chosen by ORB-SLAM, and for  $1500 \times 1500$  resolution 530 images were generated, and 146 keyframes were chosen by ORB-SLAM. The estimated camera poses, i.e., the movement of the camera through the relevant segment, as well as the corresponding sparse point cloud is shown in

<sup>5</sup><https://se.mathworks.com/help/vision/ug/monocular-visual-simultaneous-localization-and-mapping.html> (20/11-21)

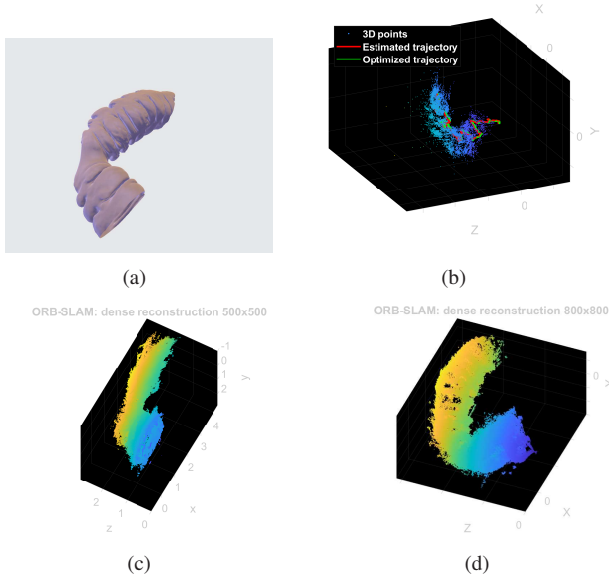


Fig. 5. ORB-SLAM output, scenario 1: (a) Ground truth colon segment (b) Estimated camera trajectory and sparse point cloud,  $500 \times 500$  resolution. (c) Dense reconstruction,  $500 \times 500$  resolution. (d) Dense reconstruction,  $800 \times 800$  resolution.

Fig. 5(b) for resolution  $500 \times 500$ . “Optimized trajectory” refers to a global optimization over all key frame camera poses after ORB-SLAM. The “ragged” trajectories captures the simulated movement obtained in VR-CAPS. The sparse cloud seems to capture the overall shape of the colon segment. The dense reconstructions in Fig. 5(c) obtained using Algorithm III-B.1, shows a clearer outline of the reconstruction, and appears to have quite similar shape to the relevant segment. However, there is quite some noise in the cloud, particularly close to the end of the segment, which is expected due to lack of loop closure. The dense reconstruction for resolution  $800 \times 800$  in Fig. 5(d) shows a clear improvement in the reconstruction, both in the overall structure, as well as in the reduction of noise. Overall, the results are quite promising.

**Scenario 2:** The colon segment under consideration is depicted in Fig. 6(a). For  $500 \times 500$  resolution, 1173 images were generated of this segment in VR-CAPS, and 332 keyframes were chosen by the ORB-SLAM algorithm for reconstruction. For  $800 \times 800$  resolution 864 images were generated, and 161 keyframes were chosen by ORB-SLAM, and for  $1500 \times 1500$  resolution 553 images were generated, and 159 keyframes were chosen by ORB-SLAM. The movement through the segment and the corresponding sparse point cloud is shown in Fig. 6(b). Again, the sparse cloud seems to capture the rough outline of the colon segment. The dense reconstruction in Figs. 6(c) and 6(d) appears to have quite similar shape to the relevant segment, most faithfully so for  $1500 \times 1500$  resolution. However, for  $500 \times 500$  resolution there is even more noise than in Scenario 1, especially after the sharp bend, which is expected due to scale- and position drift. This is not by far as critical for  $1500 \times 1500$  resolution, where scale appears to be correct throughout the whole segment. For  $500 \times 500$  resolution in particular, one can see that the cloud is denser

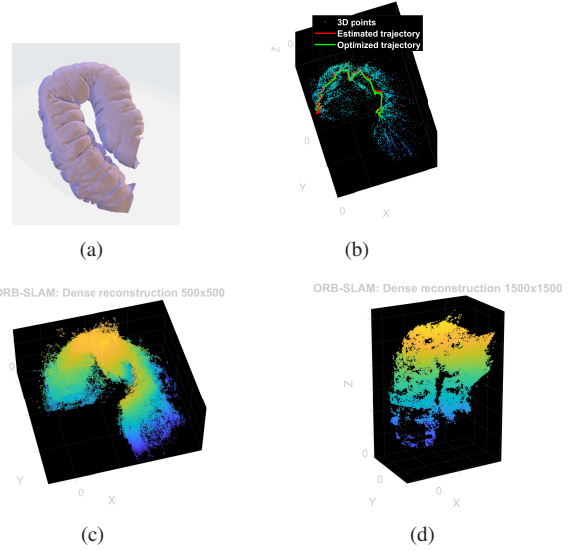


Fig. 6. ORB-SLAM output, scenario 2: (a) Ground truth colon segment. (b) Estimated camera trajectory and sparse point cloud,  $500 \times 500$  resolution. (c) Dense reconstruction,  $500 \times 500$  resolution. (d) Dense reconstruction,  $1500 \times 1500$  resolution.

on the outer side of the bend, whereas it is sparse, or lacking completely, on the inner side. The reason is that the camera is facing outwards while it moves throughout the bend. A real WCE has a fish-eye lens with a larger field of view, and so one may expect this effect to be less prominent. For  $1500 \times 1500$  resolution, these effects are much less dramatic.

**Scenario 3:** Finally, a long segment as depicted in Fig. 7(a) was tested. Resolution  $500 \times 500$  is not adequate for this scenario. For  $800 \times 800$  resolution, 1460 images were generated of this segment in VR-CAPS, and 248 keyframes were chosen by ORB-SLAM for reconstruction. For  $1500 \times 1500$  resolution, 890 images were generated, and 241 keyframes were chosen by ORB-SLAM. Image resolution is crucial as one can cope with longer segments without scale drift. For both  $800 \times 800$  and for  $1500 \times 1500$  resolution, the whole segment in Fig. 7(a) is covered quite well without significant drift.

As ORB-SLAM copes quite well with all scenarios, even sharp bends and long segments, 3D reconstruction of the human colon should indeed be possible. However, to enable reconstruction of longer segments (Scenario 3), a resolution of about  $800 \times 800$  is needed to avoid large drifts.

#### IV. SURFACE RECONSTRUCTION AND ERROR COMPUTATION

First the surface is reconstructed based on the point clouds, then the geometric deformation between the reconstructed surfaces and ground truth models is computed.

As seen in Section III, the density of the point clouds vary greatly across space, being dense in some places and nearly absent in others. The cloud is usually dense when many features are visible over several views with significant changes in parallax. Points close to the image borders are often quite sparse, and there are no points in directions not visible to the camera. The amount of detectable features will also influence



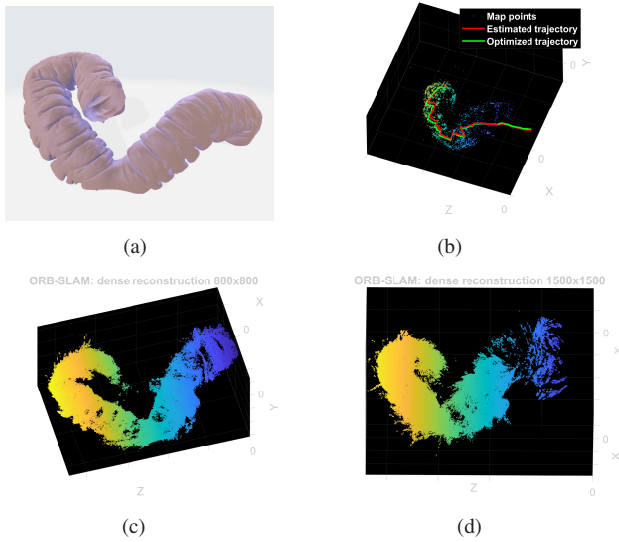


Fig. 7. ORB-SLAM output, scenario 3: (a) Ground truth colon segment. (b) Estimated camera trajectory and sparse point cloud,  $1500 \times 1500$  resolution. (c) Dense reconstruction,  $800 \times 800$  resolution. (d) Dense reconstruction,  $1500 \times 1500$  resolution.

the density, and this will depend on both the geometrical structure of the colon as well as the detail in the GI-wall texture in the relevant region. For the above-mentioned reasons, and given the fact that the colon is cylindrical in shape, it is advantageous to use a surface reconstruction method seeking a closed surface where the level of detail depends on the number of points found locally in a given region. Then regions with low density of points will be covered, but with less detail, resulting in a smoother surface. Such a reconstruction is simpler to compare with ground truth, as every region will be covered, making it unnecessary to single out regions not captured by the camera. In regions with low point density, one may alternatively mark the relevant texture to warn doctors that this is a region which is less reliable due to lack of data. Poisson surface reconstruction is a convenient solution for this problem as closed surfaces can be obtained albeit parts of  $\mathcal{X}$  being very sparse, or missing (see Section II-E).

#### A. Surface reconstruction for SLAM generated point clouds

First, Poisson surface reconstruction are applied for all three scenarios in Section III-B for image resolutions  $500 \times 500$ ,  $800 \times 800$  and  $1500 \times 1500$ . The MatLab implementation of Poisson surface reconstruction<sup>6</sup>, which is implemented according to [16], is applied here. The maximum octree depth,  $D_t$ , should be chosen so that  $8^{D_t} \sim |\tilde{\mathcal{X}}|$ , as larger values may lead to overfitting. For  $500 \times 500$ ,  $D_t = 4$  was the only viable option, while for both  $800 \times 800$  and  $1500 \times 1500$   $D_t = 5$  was the best compromise whilst  $D_t = 6$  provided more detail, but a more *ragged* structure. The densified point clouds must be denoised and downsampled so that the remaining points lie on a grid. The denoising, downsampling factor and grid-

size depends on the output point cloud from the densification procedure, and was found experimentally.

Figs. 8, 9, and 10 show all meshes generated with Poisson surface reconstruction as well as ground truth for scenarios 1, 2 and 3 respectively. From these figures one can note that as

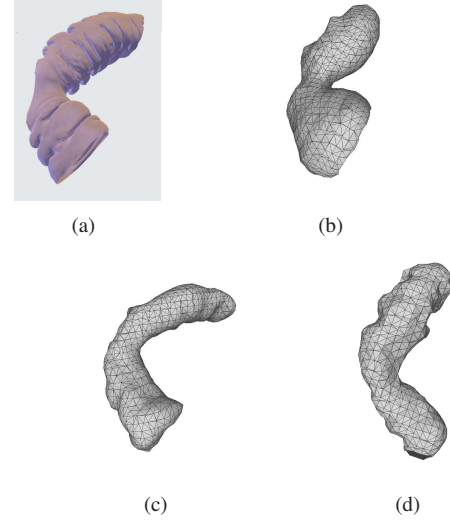


Fig. 8. Poisson surface reconstruction, scenario 1: (a) Ground truth colon segment (b)  $500 \times 500$  resolution. (c)  $800 \times 800$  resolution. (d)  $1500 \times 1500$  resolution.

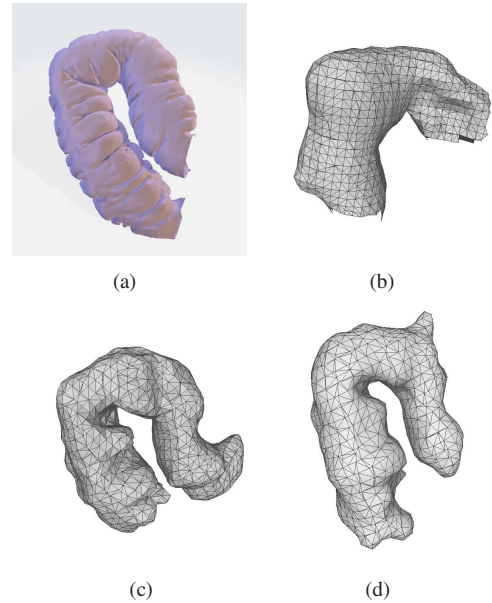


Fig. 9. Poisson surface reconstruction, scenario 2: (a) Ground truth colon segment (b)  $500 \times 500$  resolution. (c)  $800 \times 800$  resolution. (d)  $1500 \times 1500$  resolution.

pixel resolution increases, the overall structure becomes more faithful, and that the level of detail increases. Note again that the step from  $500 \times 500$  to  $800 \times 800$  pixels leads to the biggest improvement in reconstruction.

<sup>6</sup><https://www.mathworks.com/help/lidar/ref/pc2surfacemesh.html> (Nov-22)



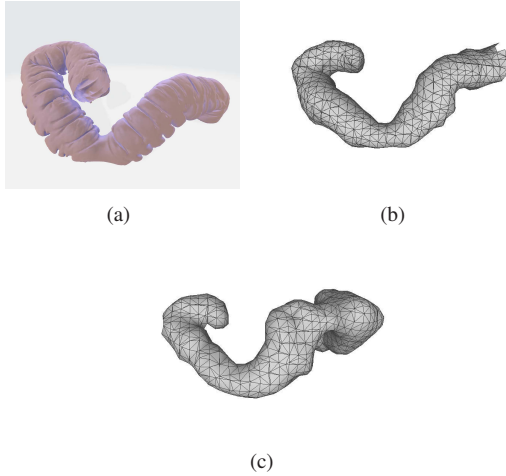


Fig. 10. Poisson surface reconstruction, scenario 3: (a) Ground truth colon segment (b)  $800 \times 800$  resolution. (c)  $1500 \times 1500$  resolution.

### B. Alignment and Error computation

Horn's method described in Section II-F is applied to align ground truth and the 3D reconstructed models. The operation is done on the mesh nodes of each model. I.e., one identifies mesh nodes of ground truth and reconstructed model with  $\mathbf{r}_{r_i}$  and  $\mathbf{r}_{l_i}$  in Section II-F (the choice is arbitrary). An implementation of Horn's method available for MatLab is the ABSOR algorithm [24], which is applied here.

The result of the alignment is shown in Fig. 11 for scenarios 1-3 for various pixel resolutions. One can observe that higher image resolution provides a better match to ground truth. Note that the ABSOR can end up in a local minimum: Take for example the result in Fig. 11(d). If the 3D reconstructed model was turned upside down the result would be a local minimum, in which a large perturbation would be needed to avoid. It is therefore important to inspect the end result to check if the models are correctly aligned. One important measure to avoid local minima, is to pre-scale the reconstructed model to a size about the same as ground truth prior to ABSOR.

With ground truth- and reconstructed models aligned, the error between them is computed in two steps: i) Resample the two surfaces uniformly so that each have approximately the same number of samples. ii) Compute the average and the max error between the models.

We use the ground truth as reference for computation. With  $L_{GT}$  ground truth points,  $\tilde{\mathbf{X}}_i = [\tilde{X}_i, \tilde{Y}_i, \tilde{Z}_i]$ , and with the reconstructed points denoted  $\hat{\mathbf{X}}_i = [\hat{X}_i, \hat{Y}_i, \hat{Z}_i] \in \hat{\mathcal{X}}$ , we compute root-mean-square error (RMSE)

$$\bar{D}_{avg(GT)} = \sqrt{\frac{1}{L_{GT}} \sum_{i=1}^{L_{GT}} \min_{\hat{\mathbf{X}}_j} \|\tilde{\mathbf{X}}_i - \hat{\mathbf{X}}_j\|_2^2} \quad (14)$$

and the max Euclidean distance

$$\bar{D}_{max(GT)} = \max_{\tilde{\mathbf{X}}_i} \left[ \min_{\hat{\mathbf{X}}_j} \|\tilde{\mathbf{X}}_i - \hat{\mathbf{X}}_j\|_2 \right], \quad (15)$$

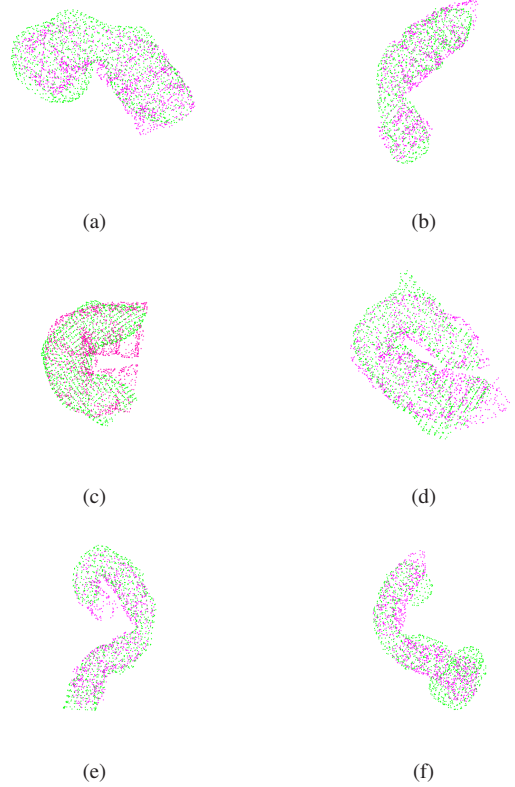


Fig. 11. Alignment of ground truth (magenta)- and 3D reconstructed (green) models: (a) Scenario 1,  $500 \times 500$  resolution. (b) Scenario 1,  $1500 \times 1500$  resolution. (c) Scenario 2,  $500 \times 500$  resolution. (d) Scenario 2,  $1500 \times 1500$  resolution. (e) Scenario 3,  $800 \times 800$  resolution. (f) Scenario 3,  $1500 \times 1500$  resolution.

where

$$\|\tilde{\mathbf{X}}_i - \hat{\mathbf{X}}_j\|_2 = \sqrt{(\tilde{X}_i - \hat{X}_i)^2 + (\tilde{Y}_i - \hat{Y}_i)^2 + (\tilde{Z}_i - \hat{Z}_i)^2}. \quad (16)$$

Since different colon segments are of different size, we also consider the *relative* RMSE which is related to the size of each 3D model. With  $\ell_{GT}$ , the length of the relevant ground truth segment measured along its center curve, we compute  $\bar{D}_{rel(GT)} = \bar{D}_{avg(GT)} / \ell_{GT}$ .

Note that the distortion measures in (14) and (15) is computed as a sequence of minimizations (or maximizations). This is to avoid the problem of sampling ground truth and reconstructed surfaces with exactly the same number of points, which can be cumbersome to obtain at the same time as one seeks to minimize distances between corresponding points. Therefore a large, but similar, number of points are scattered uniformly over each surface, then the minimum Euclidean distance to each is computed. The distortion in (14) and (15) must be used with caution: The distortion would also be relatively small for a random set of dense points over  $\mathbb{R}^3$ , or in the interior of any object covering the same region of space as the 3D model. However, with points distributed on two similar surfaces, they would have to be close overall for this measure to become small.

Table I lists the error values for the above measures for all cases and resolutions. To further analyze the error, a boxplot

| Scenario                       | RMSE  | Max Error | Relative RMSE |
|--------------------------------|-------|-----------|---------------|
| Scenario 1, $500 \times 500$   | 0.287 | 0.879     | 0.057         |
| Scenario 2, $500 \times 500$   | 0.490 | 1.34      | 0.055         |
| Scenario 1, $800 \times 800$   | 0.270 | 0.802     | 0.045         |
| Scenario 2, $800 \times 800$   | 0.390 | 1.20      | 0.043         |
| Scenario 3, $800 \times 800$   | 0.340 | 1.38      | 0.021         |
| Scenario 1, $1500 \times 1500$ | 0.230 | 0.701     | 0.038         |
| Scenario 2, $1500 \times 1500$ | 0.314 | 1.24      | 0.035         |
| Scenario 3, $1500 \times 1500$ | 0.377 | 1.09      | 0.024         |

TABLE I

ERROR TABLE FOR ALL CASES OF COLON SEGMENT 3D RECONSTRUCTION. AVERAGE (RMSE), MAX AND SCALED AVERAGE ERROR IS COMPUTED FOR  $500 \times 500$ ,  $800 \times 800$  AND  $1500 \times 1500$  IMAGE RESOLUTION.

is included in Fig. 12 for scenario 2.

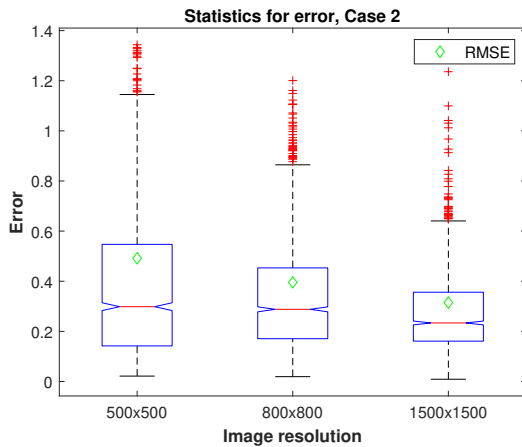


Fig. 12. Boxplot for analysis of error (RMSE) for scenario 2.

### C. Discussion on results

One can see that all three scenarios are reconstructed quite well, more faithfully so the higher the resolution. From the point clouds in Figs. 5-7 and the corresponding meshes in Figs. 8-10 it is clear that image resolution matter. This is confirmed by Table IV-B. The results in the table also reflect that colon section with sharper bends (case 2) are harder to reconstruct. However, as seen from Fig. 11 for  $1500 \times 1500$ , quite decent results can be obtained also for this case. When it comes to long sections, a resolution of at least  $800 \times 800$  is needed to get sensible results without severe scale- and position drifts. The meshes depicted in Figs. 8-10 show that quite decent reconstructions are found, even for the more irregular point clouds resulting from  $500 \times 500$  image resolution. This confirms that Poisson surface reconstruction is a convenient choice for the problem at hand. The meshes have certain false outgrowths due to erroneous points that ORB-SLAM was unable to eliminate. However, these models can be processed further in 3D modelling programs to remove obvious cases where the corresponding images show no sign of such anomalies. But in some cases, it can be difficult to determine if such outgrowths are real or not. It is important

to note that an increase in image resolution from  $500 \times 500$  to  $800 \times 800$  pixels enables reconstruction of significantly longer sections, indicating that the addition of only 300 pixels per dimension to state-of-the-art WCE sensors may be adequate to significantly improve 3D reconstruction.

From Fig. 12 one can observe that the spread in the error values is largest for  $500 \times 500$  resolution, getting smaller as the resolution increases. The large outliers (also reflected in the max error), are mostly due to areas of the ground truth colon segment not being covered. The source for these errors can be seen in Figs. 11(c) and 11(d) by comparing the green (reconstruction) and magenta (ground truth) clouds, particularly close to the ends of the segments where parts of the reconstructed cloud is missing.

Ideally the results should have been compared with other existing methods. However, from what we could find in the literature, only small parts of the colon has been reconstructed using image-based 3D reconstruction methods. More data, i.e., several more colon models, could have been exploited. However, as several practical problems, like non-rigid motion, has to be coped with before this method can be applied in a practical scenario, investigating several rigid colon models for proof-of-concept may not be worth the effort at this stage.

### V. SUMMARY AND CONCLUSIONS

In this paper, the possibility for 3D reconstruction of sections of the human colon from WCE images using ORB-SLAM has been investigated. Sections covering up to about 30% of the colon have been investigated. To generate data sets with available ground truth, a virtual graphics-based environment, named VR-CAPS, emulating both the human colon as well as the WCE's movement through it, was applied. Experimental results in this paper indicate that 3D reconstruction of the human colon is possible, becoming more accurate with increasing image resolution. Resolution is also essential when it comes to how long segments one can reconstruct before *scale drift* becomes a problem.

Poisson surface reconstruction is a suitable way of constructing surface meshes for this problem, as it can cope with point clouds with large variations in density typically arising from any feature-based 3D reconstruction algorithm applied to WCE images. Reconstruction ranging from state-of-the-art,  $500 \times 500$  pixels, to colonoscopy, about  $1500 \times 1500$  pixels, was considered. When comparing the reconstructed model to ground truth, the error reduces steadily as the pixel resolution grows. The impact is also apparent in how long segments of the colon that can be reconstructed as an increase to  $800 \times 800$  pixels makes a huge difference. This indicates that a relatively small increase in image resolution compared to the current WCE standard, makes a significant difference in facilitating 3D reconstruction.

The overarching goal of the research of this paper is to provide gastroenterologists with a personalized anatomy of any given patient, enabling enhanced viewing, localization of pathologies and planning of subsequent procedures. To fulfill this goal, future research should target extensions to more realistic scenarios, many of which can be emulated in VR-CAPS, further refining the 3D reconstruction process. In this

process, one can determine optimal pre-processing algorithms that will be applied prior to 3D reconstruction. One could also combine or merge methods studied here with single image approaches, like the effort in [6] using shape from shading, to cope with a broader scenario. Non-rigid motion often present in the GI system is of great importance to investigate to get closer to the real scenario. Further, one may eliminate drifts due to lack of loop closure in ORB-SLAM through additional information available. The WCE emits electromagnetic radiation received by several on-body sensors that can be used to track its position quite accurately [25], or compute the path length traveled [26]. This can help to correct for drift in position. Once all these features are in place one should test the approach on large data sets, both virtual ones, but most importantly real WCE videos for proof-of-concept. Future WCE may also be provided with facilities better suited for 3D reconstruction.

**1) Acknowledgements:** We would like to give our appreciation to Dr. Anuja Vats for bringing our attention to the VR-CAPS environment.

- [1] P. A. Floor, I. Farup, and M. Pedersen, "3d reconstruction of the human colon from capsule endoscope video," *IEEE Access*, vol. 13, 2025.
- [2] Editorial, "Improving uptake of colorectal cancer screening," *The Lancet Gastroenterology & Hepatology*, vol. 2, Nov. 2017.
- [3] ASGE Technology Committee, "Wireless capsule endoscopy," *Gastrointestinal Endoscopy*, vol. 78, pp. 805–815, Oct. 2013.
- [4] K. Nomura, D. Kikuchi, S. Hoteya, and T. IizukaNomura, "Three-dimensional upper gastrointestinal endoscopy: A clinical study of safety and an ex vivo study of utility in endoscopic submucosal dissection," *Gastrointestinal Endoscopy*, vol. 87, Jun. 2018.
- [5] L. Soler, S. Nicolau, P. Pessaux, D. Mutter, and J. Marescaux, "Real-time 3d image reconstruction guidance in liver resection surgery," *Hepatobiliary Surgery and Nutrition*, vol. 3, pp. 73–81, Apr. 2014.
- [6] B. Ahmad, P. A. Floor, I. Farup, and Ø. Hovde, "3D reconstruction of gastrointestinal regions using single-view methods," *IEEE Access*, vol. 11, pp. 61 103–61 117, Jun. 2023.
- [7] B. Horn and M. Brooks, "The variational approach to shape from shading," *Computer Vision, Graphics, and Image Processing*, vol. 33, pp. 174–208, Feb. 1986.
- [8] R. I. Hartley and A. Zisserman, *Multiple View Geometry in Computer Vision*, 2nd ed. Cambridge University Press, ISBN: 0521540518, 2004.
- [9] S. H. N. Jensen, M. E. B. Doest, H. Aanæs, and A. Del Bue, "A benchmark and evaluation of non-rigid structure from motion," *International Journal of Computer Vision*, vol. 129, no. 4, pp. 882–899, 2021.
- [10] V. Sidhu, E. Tretschk, V. Golyanik, A. Agudo, and C. Theobalt, "Neural dense non-rigid structure from motion with latent space constraints," in *European Conference on Computer Vision (ECCV)*, 2020.
- [11] G. Klein and D. Murray, "Parallel tracking and mapping for small ar workspaces," in *2007 6th IEEE and ACM International Symposium on Mixed and Augmented Reality*, 2007, pp. 225–234.
- [12] R. Mur-Artal, J. M. M. Montiel, and J. D. Tardós, "ORB-SLAM: A versatile and accurate monocular SLAM system," *IEEE Transactions on Robotics*, vol. 31, no. 5, pp. 1147–1163, May 2015.
- [13] K. Incetan et al., "VR-Caps: A virtual environment for capsule endoscopy," *Medical Image Analysis*, vol. 70, 2021.
- [14] P. A. Floor, I. Farup, and M. Pedersen, "3D reconstruction of the human colon from capsule endoscope video," in *Colour and Visual Computing Symposium (CVCS)*. Gjøvik, Norway: CEUR Workshop Proceedings, Sep. 2022.
- [15] B. Delaunay, "Sur la sphère vide," *Bulletin de l'Académie des Sciences de l'URSS. Classe des sciences mathématiques et na*, vol. 1934, no. 6, 1934.
- [16] M. Kazhdan, M. Bolitho, and H. Hoppe, "Poisson surface reconstruction," in *Symposium on Geometry Processing*, 2006.
- [17] B. Ahmad, P. A. Floor, I. Farup, and C. F. Andersen, "Single-image-based 3D reconstruction of endoscopic images," *Journal of Imaging*, vol. 10, no. 4, Apr. 2024.
- [18] L. Watine, P. A. Floor, M. Pedersen, P. Nussbaum, B. Ahmad, and Ø. Hovde, "Enhancement of colour reproduction for capsule endoscopy images," in *European Workshop on Visual Information Processing (EUVIP)*, Gjøvik, Norway, Sep. 2023.
- [19] M. A. Fischler and R. C. Bolles, "Random sample consensus: A paradigm for model fitting with applications to image analysis and automated cartography," *Commun. of the ACM*, vol. 24, pp. 381–395, Jun. 1981.
- [20] G. Dimas, F. Bianchi, D. K. Iakovidis, A. Karargyris, G. Ciuti, and A. Koulaouzidis, "Endoscopic single-image size measurements," *Measurement Science and Technology*, vol. 31, no. 7, pp. 9–15, May 2020.
- [21] H. Edelsbrunner, D. Kirkpatrick, and R. Seidel, "On the shape of a set of points in the plane," *IEEE Trans. Information Theory*, vol. 29, no. 4, pp. 551–559, 1983.
- [22] H. Hoppe, T. DeRose, T. Duchamp, J. McDonald, and W. Stuetzle, "Surface reconstruction from unorganized points," *SIGGRAPH Comput. Graph.*, vol. 26, no. 2, pp. 71–78, Jul. 1992.
- [23] B. Horn, "Closed-form solution of absolute orientation using unit quaternions," *Journal of the Optical Society A*, vol. 4, pp. 629–642, Apr. 1987.
- [24] J. Matt, "Absolute orientation - horn's method," in *MATLAB Central File Exchange*, Retrieved November 25, 2023. [Online]. Available: <https://www.mathworks.com/matlabcentral/fileexchange/26186-absolute-orientation-horn-s-method>
- [25] B. Moussakhani, J. T. Flåm, S. Støa, I. Balasingham, and T. Ramstad, "On localisation accuracy inside the human abdomen region," *IET Wireless Sensor Systems*, vol. 2, no. 1, pp. 9–15, Mar. 2012.
- [26] A. Bjørnevik, P. A. Floor, and I. Balasingham, "On path length estimation for wireless capsule endoscopy," in *12th International Symposium on Medical Information and Communication Technology (ISMICT)*, 2018, pp. 1–5.